AIAA JOURNAL
Vol. 38, No. 9, September 2000

Computational Aeroacoustic Analysis of Slat Trailing-Edge Flow

Bart A. Singer,* David P. Lockard,† and Kenneth S. Brentner‡
NASA Langley Research Center, Hampton, Virginia 23681-2199

An acoustic analysis based on the Ffowcs Williams and Hawkings equation (Ffowcs Williams, J. E., and Hawkings, D. L., "Sound Generated by Turbulence and Surfaces in Arbitrary Motion," *Philosophical Transactions of the Royal Society of London*, Vol. A264, No. 1151, 1969, pp. 321–342) was performed for a high-lift system. As input, the acoustic analysis used unsteady flow data obtained from a highly resolved, time-dependent, Reynolds-averaged Navier–Stokes calculation. The analysis strongly suggests that vortex shedding from the trailing edge of the slat results in a high-amplitude, high-frequency acoustic signal similar to that which was observed in a corresponding experimental study of the high-lift system.

Nomenclature

C = cruise-wing chord
c = ambient speed of sound
d = observer distance to slat trailing edge
f = function describing integration surface
$H(\cdot)$ = Heaviside function
h = slat trailing-edge thickness
L_i = term defined in Eq. (3)
L_z = half-span
$\hat{n}_j$ = component of unit normal vector
P_{ij} = compressive stress tensor
p' = acoustic pressure
T_{ij} = Lighthill stress tensor
t = observer time
U_i = term defined in Eq. (2)
u_i = velocity component of flow
v_i = velocity component of integration surface
x = streamwise coordinate
$\boldsymbol{x}$ = observer position vector
z = spanwise coordinate
$\delta(\cdot)$ = Dirac delta function
δ_{ij} = Kronecker delta
ρ = density
ρ' = perturbation density
$\Box^2$ = wave operator

Subscripts

n = projection of a vector quantity in the surface-normal direction
0 = freestream quantity

Introduction

AIRFRAME-GENERATED noise is an important component of the total noise radiated from commercial aircraft, especially during the approach portion of the flight path. Studies by Davy and Remy[1] on a scale-model Airbus aircraft indicate that the high-lift devices and landing gear are the main sources of airframe noise when the aircraft is configured for approach. Earlier tests on a model of a DC-10 also identified the high-lift system as an important airframe noise source.[2] Full-scale experimental studies of a portion of a wing equipped with a high-lift system, performed in an open-jet wind tunnel by Dobrzynski et al.,[3] revealed that both the leading-edge slat and the side edge of the trailing flap contributed significantly to the airframe noise.

At NASA Langley Research Center an extensive experimental and computational effort to study the various mechanisms associated with airframe-generated noise[4] has made considerable progress in understanding various aspects of the noise-generation process on the flap-side edge[5–11] and in the vicinity of the leading-edge slat.

A cooperative test involving NASA's high-lift program element and NASA's airframe noise team was conducted in NASA Langley Research Center's low-turbulence pressure tunnel (LTPT). Variation of the pressure in the tunnel allows the Reynolds number to be changed at constant Mach number. In these tests, the Reynolds number based on the cruise-wing chord (0.55 cm) varied from 3.6×10^6 to 19×10^6. No qualitative changes were observed in the data for Reynolds numbers above 7.2×10^6. The model tested in the tunnel is known as the energy-efficient transport (EET) model.[12] The EET model tested includes a full-span leading-edge slat and a part-span trailing flap. To obtain acoustic data, members of Boeing Commercial Airplane Company designed and built a microphone array that was then installed in the ceiling of the wind tunnel. The microphone array and the subsequent data processing followed techniques developed earlier at Boeing.[13] These techniques had previously been used successfully to determine the noise radiated from localized sources, even in hard-walled, nonanechoic wind tunnels like the LTPT. To measure noise radiating groundward in normal flight, the EET model was mounted upside down in the tunnel so that the pressure surface faced the acoustic microphone array in the wind-tunnel ceiling. However, to reduce confusion, all references to directions in this paper will conform to the schematic of the experimental setup shown in Fig. 1. The view in Fig. 1 has been rotated from the physical orientation to one that is more intuitive. An enormous amount of data was collected and analyzed. In Fig. 1, flow is from left to right, and acoustic directivity angles 0 and 270 deg are indicated.

Figure 2 illustrates one unexpected feature of the experimental data. For the case in which the slat deflection δ_s is 30 deg, a very large-amplitude peak is observed in the acoustic spectrum in the vicinity of 50 kHz. This peak rises about 20 dB above the signal observed for the case in which the slat is deflected 20 deg. During the course of the experiment, efforts to eliminate the high-frequency peak by altering the overhang of the slat were largely unsuccessful. Only for cases in which the overhang became unrealistically large was a significant change in the high-frequency acoustic peak observed. Increasing the configuration's angle of attack from 10 to 15 deg reduced the amplitude of the high-frequency peak by approximately 10 dB. Similar experimental variations were reported by Storms et al.[14] For some time, no consistent explanation of the observed phenomenon was available. The focus of this paper is to explain the observed large-amplitude, high-frequency peak in the experimentally obtained acoustic spectrum.

Khorrami et al.[15] provide details of unsteady, two-dimensional, Reynolds-averaged Navier–Stokes (RANS) calculations designed

Received 4 June 1999; revision received 19 February 2000; accepted for publication 19 February 2000.

*Research Scientist, Computational Modeling and Simulation Branch.
†Research Scientist, Computational Modeling and Simulation Branch. Senior Member AIAA.
‡Senior Research Engineer, Computational Modeling and Simulation Branch. Senior Member AIAA.

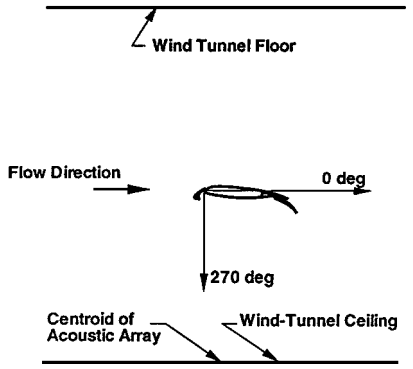

Fig. 1 Schematic of model in wind tunnel.

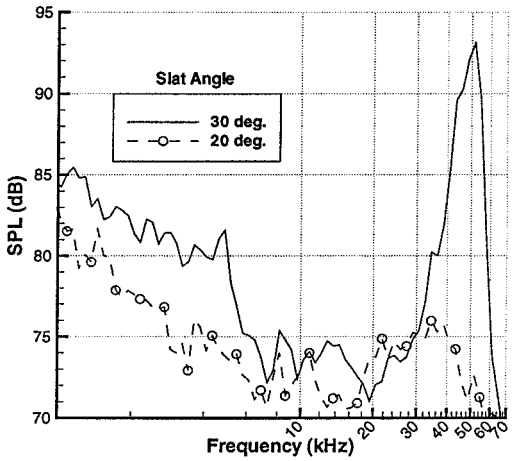

Fig. 2 Acoustic spectrum based on $\frac{1}{12}$th octave bins with array focused on slat region: configuration angle of attack is 10 deg, Reynolds number is 7.2×10^6, and Mach number is 0.2.

to mimic the experimental conditions. The calculations were performed with a wind-tunnel speed of 70 m/s, which was appropriate for matching the nominal Mach number of 0.2 in the experiments. In addition, the RANS computation was specially designed to incorporate properly and resolve the small but finite trailing-edge thickness of the slat. Extremely small grid cells were used in the vicinity of the slat trailing edge, and the time step was chosen to ensure more than 120 time steps per period of a 50-kHz signal. Initially, calculations were performed with a slat trailing-edge thickness h of approximately 0.07% of the cruise-wing chordlength C, which was an estimate of the actual slat trailing-edge thickness. Slat deflections of both 30 and 20 deg were simulated. These calculations clearly showed vortex shedding from the slat trailing edge for the case with a 30-deg slat deflection. Figure 3 shows a snapshot of the pressure fluctuations produced in the flowfield. The dark and light bands indicate instantaneous reductions and increases in pressure in comparison with the local time-averaged pressure. The vortex shedding virtually disappears for the case of a 20-deg slat deflection. For a somewhat different, three-element high-lift model, Storms et al.[14] observed a completely laminar boundary layer on the slat suction surface for their high slat-deflection case, but not for their lower slat-deflection cases. Here all of the calculations were performed with the flow assumed to be fully turbulent; hence, the differences cannot be attibuted to laminar flow in one case and turbulent flow in the other. Acoustic analyses of the early computational results suggested that the initial grid distribution was insufficient to resolve completely the complex acoustic field in the cove and other regions in the vicinity of the slat. Later calculations with an enhanced grid were performed for a 30-deg slat deflection with $h/C \approx 0.0009$. The slat thickness was adjusted in these latter calculations to represent more accurately the measured slat thickness on the model. In all cases, the high cost of the calculations limited the duration of the temporal sample that was obtained. Here we discuss the use of that limited sample of unsteady computational data to perform acoustic analyses of the generated noise.

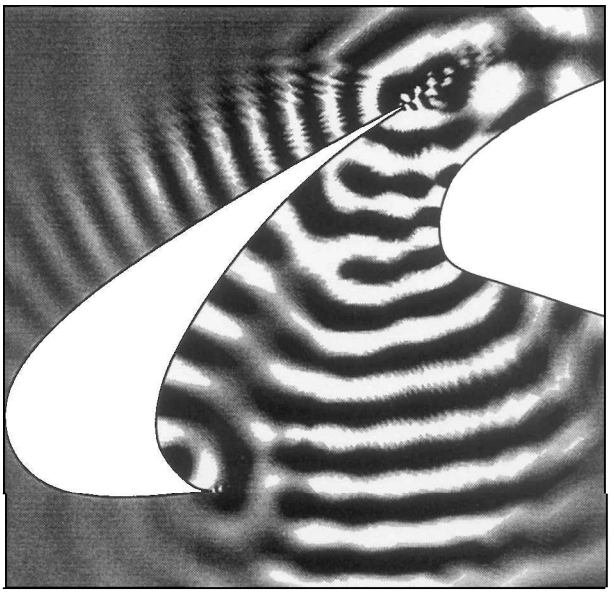

Fig. 3 Instantaneous fluctuation pressure in vicinity of leading-edge slat from CFD calculation: slat deflection is 30 deg, and wiggles at edges of dark and light bands are contouring artifacts.

Acoustic Procedure

Previously, Singer et al.[16] explored the use of unsteady computational data in acoustic-propagation codes based on the Ffowcs Williams and Hawkings[17] (FW–H) equation. Such codes compute the acoustic signal at a distant observer position by integrating the FW–H equation. Following Brentner and Farassat,[18] the FW–H equation may be written in differential form as

$$\Box^2 p'(\boldsymbol{x}, t) = \frac{\partial^2}{\partial x_i \partial x_j}[T_{ij} H(f)] - \frac{\partial}{\partial x_i}[L_i \delta(f)] + \frac{\partial}{\partial t}[(\rho_0 U_n)\delta(f)] \tag{1}$$

where

$$\Box^2 \equiv \frac{1}{c^2}\frac{\partial^2}{\partial t^2} - \nabla^2$$

is the wave operator, c is the ambient speed of sound, t is observer time, p' is the acoustic pressure, ρ' is the perturbation density, ρ_0 is the freestream density, $f = 0$ describes the integration surface, $\delta(f)$ is the Dirac delta function, and $H(f)$ is the Heaviside function. The quantities U_i and L_i are defined as

$$U_i = (1 - \rho/\rho_0)v_i + \rho u_i/\rho_0 \tag{2}$$

$$L_i = P_{ij}\hat{n}_j + \rho u_i(u_n - v_n) \tag{3}$$

respectively. In the preceding equations, ρ is the total density, ρu_i is the momentum in the i direction, v_i is the velocity of the integration surface $f = 0$, and P_{ij} is the compressive stress tensor. For an inviscid fluid, $P_{ij} = p'\delta_{ij}$, where δ_{ij} is the Kronecker delta. The subscript n indicates the projection of a vector quantity in the surface-normal direction. To obtain a solution to Eq. (1), the first term on the right-hand side must be integrated over the volume outside the integration surface $f = 0$ wherever the Lighthill stress tensor T_{ij} is nonzero in this region. In the work reported here, this term is neglected. However, the main effects of nonzero T_{ij} within the flow can be included by choosing an integration surface that contains all of the volume with significant T_{ij} contributions.

The other terms on the right-hand side of Eq. (1) include terms that are determined by the unsteady flowfield data on the integration surface. Singer et al.[16] demonstrate that, provided the unsteady flow data on the integration surface $f = 0$ is accurate, the FW–H equation correctly propagates the acoustic radiation, including the complex signals associated with acoustic scattering from sharp edges. Similarly, other researchers have found that RANS data can provide sufficiently accurate input. Cox et al.[19] performed time-dependent

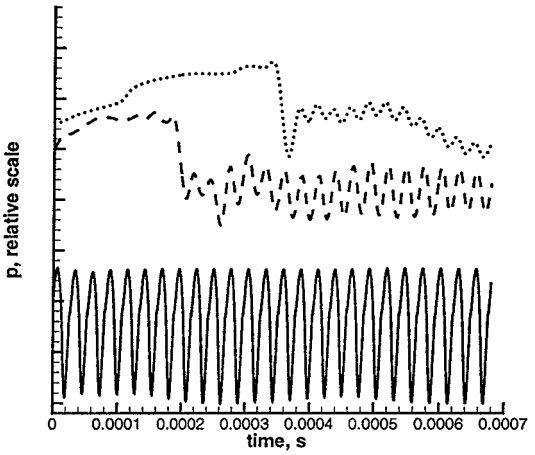

Fig. 4 Perturbation pressure as function of time: slat deflection is 30 deg; ——, slat trailing edge; – – –, slat cusp (scaled ×40); and · · · ·, slat leading edge (scaled ×200).

RANS calculations for flow over a circular cylinder and used the unsteady results as input for the solution of the FW–H equation. Their results away from the critical Reynolds number range are consistent with experimental observations when an appropriate spanwise correlation length is used. Rumsey et al.[20] coupled time-dependent RANS calculations to acoustic-propagation codes for the complicated problem of ducted fan flow. Their results for the single acoustic mode targeted in their study showed acceptable agreement with experiment. These works suggest that carefully performed RANS calculations are capable of providing sufficiently accurate input for acoustic-propagation codes, especially in cases where the acoustic sources are well defined.

The extremely small time step required in the RANS calculation to resolve the high-frequency flow physics adequately resulted in a limited temporal duration of the data. The total time represented by the unsteady calculation was 0.68 ms, approximately long enough for an acoustic wave generated at the leading edge of the main element to propagate halfway down the cruise-wing chord C. Because of the short time duration, the potential importance of the initial transient is assessed. Figure 4 shows the perturbation pressure signal at the slat trailing edge, the slat cusp, and the slat leading edge. To account for the rapidly decaying amplitude of the fluctuating pressure relative to the scale of the pressure fluctuations at the slat trailing edge, the scale of the pressure fluctuations is magnified by a factor of 40 at the slat cusp and a factor of 200 at the slat leading edge. Although the data at the slat trailing edge are quasi periodic from the start, over 0.2 ms pass before the transient goes by the slat cusp and almost 0.38 ms pass before the transient propagates past the slat leading edge. The early establishment of periodicity at the slat trailing edge is a consequence of its proximity to the shed vortices. After passage of the initial transient, a quasi-periodic condition prevails at all locations. To limit the effect of the transient, the first 25% of the data record was not used to produce the results presented here. Auxiliary calculations suggested that the use or nonuse of the first 25% of the data record produced relatively small quantitative variations in the results, and all of the qualitative results were unchanged. Therefore, the initial transient appears to be unimportant for the results of the analysis. However, further reduction in the size of the data record (so that only the last 50% of the data is used) results in more significant quantitative changes, especially in the lower frequencies. Tests with analytically defined sources reveal that the data-windowing procedure described hereafter has a noticeable effect on the results when the time records contain fewer than about 15 cycles of the dominant frequency. To preclude any confusion, hereafter the term data record or any equivalents should be construed to refer to only the portion of the data that was actually used.

To deal with the limited data time series, a modified Hanning window was applied to the data. The modified Hanning window included a standard Hanning filter for the first and last 12.5% of the data and a boxcar filter for the middle 75%. The windowed data was scaled to preserve the original energy in the signal. The resulting data sequence was then implicitly repeated as needed to provide an input signal of arbitrary duration. The windowing created an artificial periodicity at approximately 1960 Hz, but because this frequency was much lower than the vortex shedding frequency, the artificial periodicity did not introduce any problems.

The application of acoustic theories to two-dimensional flow data is a problem that is likely to become more visible as computational fluid dynamics (CFD) is relied on more regularly to provide unsteady flow data for use in acoustic calculations. Time-dependent, three-dimensional CFD data is extremely expensive to produce. In many applications, as in the current problem, the primary aerodynamic phenomena that generate noise are essentially two dimensional. The three-dimensional effects are largely caused by the limited correlation of the true three-dimensional unsteady flow structure in the third direction. Cox et al.[19] computed two-dimensional and three-dimensional vortex shedding over circular cylinders and then used the results to calculate the acoustic pressure at an observer location. To use the two-dimensional CFD computations, the acoustic calculations were performed by assuming perfect spanwise correlation of the flow over a finite span. They found that the acoustic amplitude could increase by as much as 20 dB simply by extending the finite span from 5 to 100 cylinder diameters.

As a first approximation, a two-dimensional version of the FW–H equations was used in the present study to predict the sound field. Here we used the code developed by Lockard[21] for computing the two-dimensional acoustic field from two-dimensional CFD data. As noted, we expected the two-dimensional results to have greater amplitudes than those observed in the experiment, but the qualitative features of the acoustics were not expected to differ substantially. To study the effects of the spanwise correlation length, a limited number of three-dimensional acoustic calculations were performed with the same FW–H code as was used in Ref. 16. As input to the three-dimensional code, the two-dimensional CFD data was repeated for a finite distance in the spanwise direction. (Previous tests on idealized problems confirmed that the three-dimensional FW–H code and the two-dimensional FW–H code give identical results for model problems when the spanwise extent in the three-dimensional problem is sufficiently long.)

For consistency, all of the acoustic calculations were performed for observers located a fixed distance from the trailing edge of the slat. The fixed distance corresponded to the distance from the slat trailing edge to the centroid of the acoustic array. Directivity angles are indicated in Fig. 1; 0 deg is in the downstream direction, 270 deg is groundward in normal flight, toward the microphone array in the wind tunnel.

Another important issue involved the choice of integration surface for the FW–H calculation. Figure 5 illustrates the two integration surfaces that have been used for the FW–H calculations for the cases with a slat trailing-edge thickness $h/C \approx 0.0007$. The solid lines correspond to the component surfaces that lie on the solid bodies of the slat and main element. This combination of surfaces is designated the on-body surface. Because the limited time sample is insufficient for acoustic signals to propagate from the leading-edge slat to the trailing flap, the information on the flap is not included. If it were included, it would contribute almost nothing to the noise; the computations show that the flow in the vicinity of the flap is steady. The dotted line corresponds to a permeable mathematical surface that contains within it the boundary layers on all three elements of the high-lift system as well as the region where the shed vortices reside. This integration surface includes all of the major

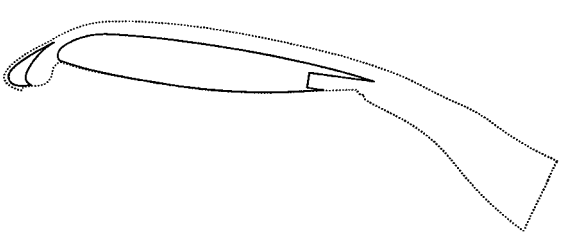

Fig. 5 Integration surfaces used for FW–H calculations with $h/C \approx 0.0007$: ——, on-body surface, and · · · ·, off-body surface.

noise sources in this flow and is designated the off-body surface. Because the flowfield quadrupole contributions to the noise are substantially contained within the off-body surface, the neglected T_{ij} term in Eq. (1) is essentially zero for this case, and little error is introduced by not integrating the term explicitly. Although this consideration suggests that the off-body surface is a better choice than the on-body surface, in practice CFD grid resolution issues complicate the choice. Because of the limited order of accuracy of the CFD calculations,[15] flow fluctuations present on the on-body surface may have been numerically dissipated and dispersed by the CFD calculations before the fluctuations arrive on the off-body surface, especially in the region between the pressure surface of the slat and the leading edge of the main element.

The deficiencies in the CFD grid between the slat and the main element have been minimized by refining the grid for the calculation with the slat trailing-edge thickness $h/C \approx 0.0009$. In addition, our experience with the prior calculations suggested that data be saved on a number of additional integration surfaces. Close-up views of these integration surfaces in the vicinity of the slat are shown in Figs. 6 and 7. For convenience, the five integration surfaces used for the $h/C \approx 0.0009$ case are labeled 0–4. A brief description of each surface is given in Table 1. In Fig. 6 the solid lines (surface 0) represent the physical surfaces and correspond to the on-body integration surfaces as used in the $h/C \approx 0.0007$ cases. The dash-dot-dot lines (surface 4) extend outside of the slat and main element boundary layers, but do not include the cove region. Because the flow is separated on the pressure side of the slat, the boundary layer is poorly defined in this region; hence, the slat pressure side of surface 4 is simply a near-wall surface. The dotted lines (surface 3) indicate a

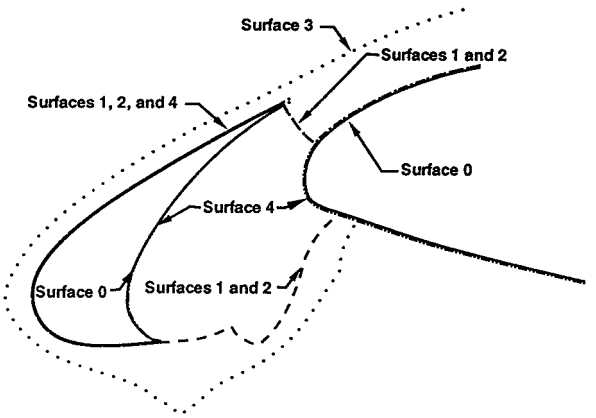

Fig. 6 Integration surfaces used for FW–H calculations with $h/C \approx 0.0009$: ——, on-body (surface 0); – – –, outside of boundary layers and cove (surfaces 1 and 2; see Fig. 7 to distinguish); · · · ·, far outside of wakes and boundary layers (surface 3); and – · –, outside of boundary layers but not including cove.

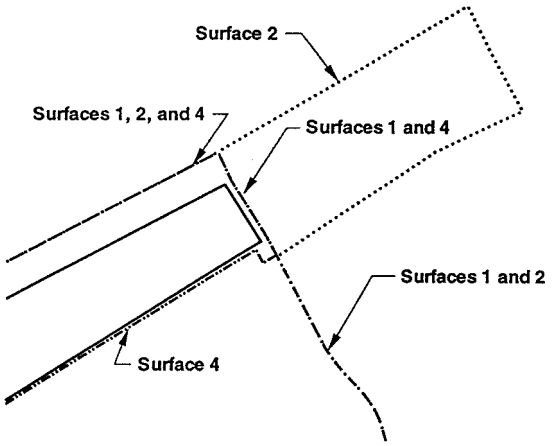

Fig. 7 Close-up view of slat trailing edge: ——, surface 0; – – –, surface 1, · · · ·, surface 2; and – · –, surface 4. (Surfaces 1 and 2 share boundaries away from slat trailing edge, and some boundaries are also shared with surface 4.)

Table 1 Description of integration surfaces

Surface	Description
0	On body
1	Off body, just outside boundary layers and cove
2	Includes surface 1 and small region behind slat trailing edge
3	Far outside of all wakes and boundary layers
4	Off body, just outside boundary layers

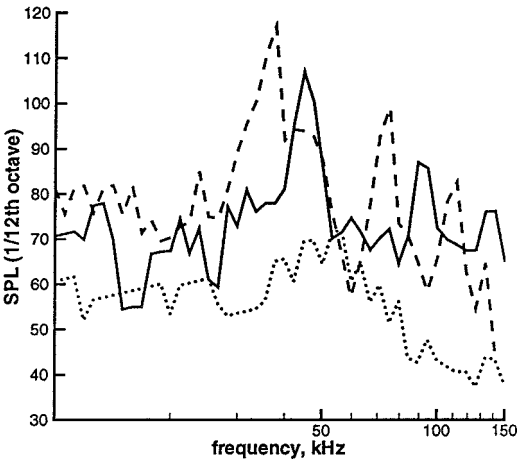

Fig. 8 Spectra for observer positioned at 270 deg by using on-body integration surfaces: ——, 30-deg slat deflection, $h/C \approx 0.0007$; · · · ·, 20-deg slat deflection, $h/C \approx 0.0007$; and – – –, 30-deg slat deflection, $h/C \approx 0.0009$.

surface that includes all boundary layers and wakes and corresponds closely to the off-body integration surface used in the $h/C \approx 0.0007$ cases. The dashed lines (surfaces 1 and 2) are intermediate surfaces that extend just outside of the boundary layers and include the entire cove region between the slat and main elements. The distinction between surfaces 1 and 2 is shown in Fig. 7. Surface 1 (shown with the dashed line) does not include the shed vortices in the wake of the slat. In contrast, surface 2 (shown with the dotted line) includes a region that contains a limited number of the shed vortices. Surfaces 1 and 2 are believed to offer the most reasonable compromise between inclusion of acoustic sources and adequate CFD grid resolution from the sources to the integration surfaces.

Although the FW–H equation does not require that the integration surfaces be smooth, nonsmooth integration surfaces degrade the numerical accuracy of the integration. To address whether this might be a problem, the acoustic results obtained by using all of the available integration points on surface 1 were compared with the results obtained by using half of the available integration points. The difference in the acoustic pressure for each of 360 observers was never more than 10% of the full-resolution value and was typically less than 4%.

Results

Figure 8 shows computed spectra based on $\frac{1}{12}$th octaves for an observer located at 270 deg. Only results for the on-body integration surfaces are shown. The number of cycles in the data record for frequencies below about 30 kHz is insufficient for drawing reliable conclusions in that range. In addition, for the slat deflection of 20 deg, the small-amplitude peak around 45 kHz is a residue of the initial transient. The analysis of the data in Ref. 15 shows no sustained vortex shedding in the CFD flow results for the 20-deg slat deflection. The corresponding FW–H spectrum shows that no significant noise radiates for the 20-deg slat deflection. On the other hand, the vortex shedding associated with the 30-deg slat deflection produces intense noise, peaking at around 45 kHz for the $h/C \approx 0.0007$ case and at about 38 kHz for the $h/C \approx 0.0009$ case. Figure 9 shows the spectra for both trailing-edge thicknesses when comparable off-body integration surfaces are used. The dominant frequencies and general trends remain unchanged. As expected, the thicker slat trailing edge results in stronger disturbances and louder noise levels. The lower frequency peak for the thicker trailing edge is consistent

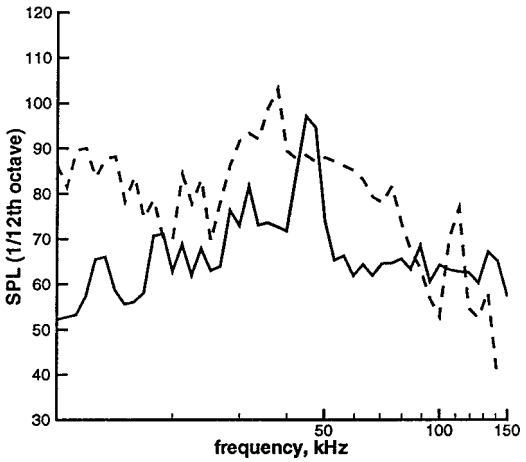

Fig. 9 Spectra for observer positioned at 270 deg by using off-body integration surfaces with 30-deg slat deflection: ——, $h/C \approx 0.0007$, and – – –, $h/C \approx 0.0009$.

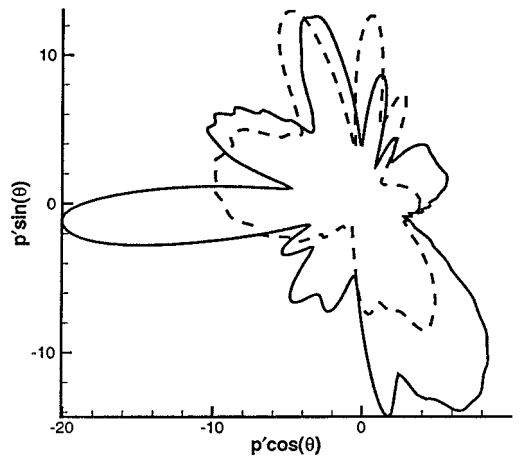

Fig. 10 Directivity of acoustic signal for $h/C \approx 0.0007$: ——, on-body surface, and – – –, off-body surface.

with the expectation of Strouhal scaling for the vortex shedding. However, the 27% increase in trailing-edge thickness results in approximately a 16% decrease in dominant frequency. Clearly, the trailing-edge thickness is not the only important flow parameter. Hammond and Redekopp[22] suggest the use of the body thickness plus the displacement thicknesses as the appropriate length scale for Strouhal scaling. Examination of the CFD data supports this suggestion. When the displacement thickness was estimated as one-seventh of the boundary-layer thickness and the boundary-layer thickness taken as the distance from the surface at which the total pressure was approximately that of the freestream total pressure, the length scale based on slat trailing-edge thickness plus estimates for the upper and lower boundary-layer displacement thicknesses increased approximately 19% for the thicker slat trailing edge. Therefore, the Strouhal number based on this length scale remained approximately constant for the different trailing-edge thicknesses.

Although the frequency of maximum noise does not vary with differing integration surfaces, the directivity pattern does. Figure 10 shows directivity patterns for the on- and off-body integration surfaces with $h/C \approx 0.0007$. In Fig. 10, at any angle, the distance from the origin is proportional to the integrated pressure spectrum that radiates at the chosen angle. Because the noise is dominated by the high-frequency tone, integrating over all frequencies gives a directivity pattern that is indistinguishable from that obtained by just integrating the contributions from the frequencies in the vicinity of the tone. The solid line represents the directivity computed with CFD data on the on-body surface, whereas the dashed line represents the directivity computed with the CFD data from the off-body surface. Significant qualitative differences exist, especially with regard to the strong upstream and downward directivity projections associated with the on-body integration surface. Without experimental

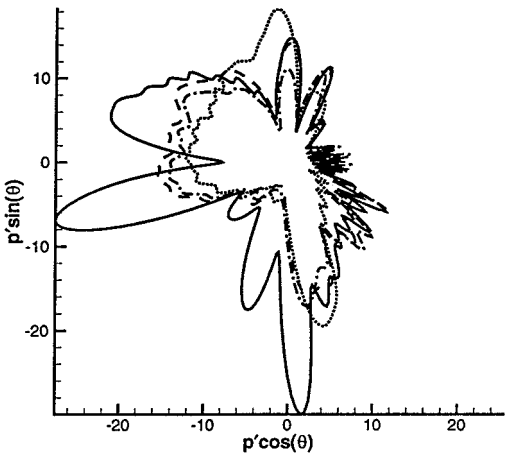

Fig. 11 Directivity of acoustic signal for $h/C \approx 0.0009$: ——, on-body surface (surface 0); – – –, surface 1; – –, surface 2; and · · · ·, surface 3.

directivity measurements or another calculation that better resolves the acoustic signals in the region between the on- and off-body integration surfaces, choosing which integration surface provides the more realistic prediction is difficult. Fortunately, the $h/C \approx 0.0009$ calculation provides adequate grid resolution to a variety of off-body surfaces.

Figure 11 shows the directivity patterns that are obtained from the integration surfaces used with the thicker trailing-edge case. Many features of the directivity patterns are similiar for both the $h/C \approx 0.0007$ calculation and the $h/C \approx 0.0009$ calculation. In particular, for the on-body integration surfaces, strong noise radiation is directed slightly above and below 180 deg and at approximately 90, 225, and 270–300 deg. These strong directivity projections exist for both slat trailing-edge thicknesses. As would be expected, the presence of the main element blocks significant acoustic radiation in the downstream direction. The use of off-body integration surfaces has a similar effect for both trailing-edge thickness cases. The strong upstream-directed projections slightly above and below 180 deg, which are associated with the on-body integration surfaces, merge and have reduced levels. The acoustic radiation peak directed at approximately 225 deg essentially disappears when off-body integration surfaces are used, and the strong downward-directed acoustic radiation is reduced in amplitude.

In Fig. 11 the directivity patterns for off-body surfaces 1–3 are generally similar. However, where differences occur, simple explanations or trends are lacking. For instance, surface 3, which includes the entire slat wake, suggests stronger radiation in the 90–120 deg range than either surface 1 or 2. However, the use of surface 2, which includes some of the slat wake, results in less acoustic radiation in this region than does the use of surface 1, which includes none of the slat wake. Therefore, no clear trend exists with respect to the inclusion of additional portions of the slat wake.

The different directivity patterns obtained with the on-body surface and the various off-body surfaces raise the question as to whether the differences are primarily associated with the boundary layers in the slat cove region. To help resolve this question, directivity patterns obtained from integration surface 4 are compared in Fig. 12 with those obtained from the on-body integration surface. Surface 4 shares extensive regions outside of the boundary layers with surfaces 1 and 2; however, surface 4 differs from surfaces 1 and 2 in that it does not enclose the slat cove region (see Figs. 6 and 7). The similarity between the patterns in Fig. 12 suggests that acoustic contributions from the slat cove region are responsible for most of the differences observed in Figs. 10 and 11.

Although the acoustic array used in the experiment was not intended to provide any directivity information, the high-frequency acoustic signal was so loud that it overwhelmed the intrinsic wind-tunnel noise and can be identified from the spectrum of some of the individual microphones used in the acoustic array. Figure 13 shows the relative amplitudes of the mean square fluctuating pressure in a frequency range around 50 kHz from a subset of microphones having approximately the same cross-stream location. The abscissa in

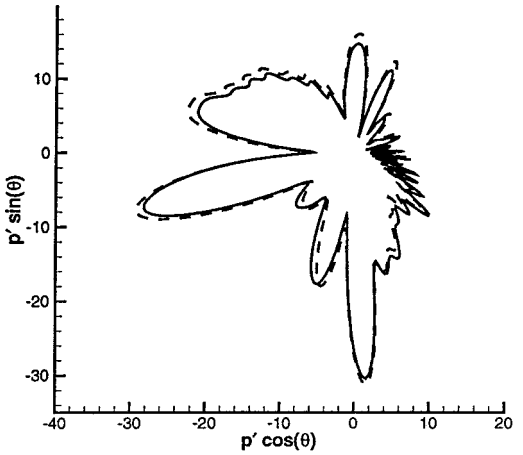

Fig. 12 Directivity of acoustic signal for $h/C \approx 0.0009$: ——, on-body surface (surface 0), and - - -, surface 4.

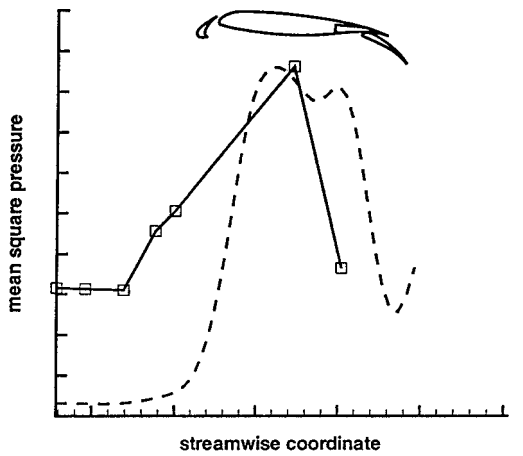

Fig. 13 Squared acoustic pressure at individual microphones compared to that predicted computationally for $h/C \approx 0.0009$ case by using integration surface 1. (Squares indicate microphone positions and values, dashed line indicates computationally predicted values.)

Fig. 13 indicates streamwise distance. The microphone locations are shown as squares in Fig. 13, and their positions relative to the airfoil are easily deduced. The computed mean-square fluctuating pressure projected to the acoustic-array surface is shown as the dashed line. The computed results are calculated by the use of integration surface 1. The maximum amplitude of the microphone data is scaled with the maximum amplitude of the calculation. Far upstream of the airfoil, both the microphone response and the computed noise level are flat. The nonzero microphone response is probably associated with the wall-pressure fluctuations of the turbulent boundary layer along the wind-tunnel ceiling. These fluctuations are not included as part of the CFD calculations. Slightly upstream of the slat leading edge, the noise level rises. Unfortunately the construction of the wind tunnel prevented the positioning of microphones over an extensive region that would include the streamwise location of the slat trailing edge. The maximum amplitude occurs in the midchord region and is followed by a sharp drop in amplitude. The qualitative features of the computations agree remarkably well with the microphone data and have been used to aid in the redesign of the acoustic array for a future wind-tunnel test.

In the actual flow, the vortex-shedding process is not perfectly correlated in the spanwise direction. The correlation between two points is reduced as the spanwise distance between them increases. The physical decorrelation process could be modeled as a random walk; however, numerical integration over a very large distance in the spanwise direction would then be required. In this study, we model the effects of the span by assuming perfect correlation along a fixed spanwise distance, with no contribution from points outside of this distance. The half-span used in the calculations is denoted by L_z, and it is normalized with the cruise-wing chord C. The observers are positioned a distance $d = 2C$ from the slat trailing edge.

To estimate the sort of behavior that we might expect for the three-dimensional acoustic calculation, we first examine the analytically predicted behavior of a continuous line source in the spanwise direction. For this source, the contribution to the pressure will vary in the spanwise direction as

$$\left[1/\sqrt{1+(z/d)^2}\right]\exp\left[i\omega d/c\sqrt{1+(z/d)^2}\right] \tag{4}$$

where z is the spanwise coordinate and the observer is located at $z = 0$. The leading factor $1/\sqrt{[1+(z/d)^2]}$ controls the decay of the amplitude of the acoustic contribution as the source points move away from the observer. The terms in the exponential determine the spatial periodicity. For small values of z, the spanwise oscillation period is large, but the period decreases with increasing z. To reduce the spanwise oscillation amplitude to 10% of its $z = 0$ value requires that $z \approx 10d$, or, for the cases studied here, about 11 m. This distance is far greater than the wind-tunnel span and would clearly be much greater than any reasonable estimate of the spanwise coherence. These estimates suggest that the two-dimensional calculations are likely to overpredict substantially the amplitude of the acoustic field. Further analysis of Eq. (4) suggests that near $z = 0$, the spanwise oscillation period z_p for a 38-kHz source is $z_p/C \approx 0.26$, but that for large values of z, the oscillation period is much smaller, with $z_p/C \approx 0.015$. The variation of the oscillation period requires that spanwise grid-resolution requirements be reviewed whenever the spanwise extent changes.

Because three-dimensional acoustic calculations are much more expensive than their two-dimensional counterparts, 36 observers (spaced 10 deg apart) were used in an initial set of three-dimensional acoustic calculations to determine trends with variation of the spanwise extent L_z. Only data on integration surface 1 were used for these calculations. After ascertaining the spanwise resolution requirements and finding no unexpected tendencies, acoustic calculations with $L_z/C = 0.25$ and 2.0 were performed with 180 observers spaced 2 deg apart. The directivity patterns are compared with the results from the two-dimensional calculation in Fig. 14.

Examination of Fig. 14 reveals some interesting trends. As expected, with increased spanwise extent the noise increases. Additional cases run with $0.25 < L_z/C < 2.0$ show that the increase in noise is not monotonic, varying instead with the spanwise period. Cox et al.[19] observed a similar trend until, at some value of L_z, the average noise level asymptoted and only small variations associated with the periodicity in z were observed. Our data suggest that the qualitative features of even a complex directivity pattern establish themselves at relatively small values of L_z. In Fig. 14, all of the directivity lobes found in the two-dimensional results can be traced back to corresponding lobes obtained with both $L_z/C = 2.0$ and 0.25. Recall that $L_z/C \approx 0.26$ corresponds to the spanwise period in Eq. (4) for $z \approx 0$; therefore, the basic directivity features are established within the first spanwise period.

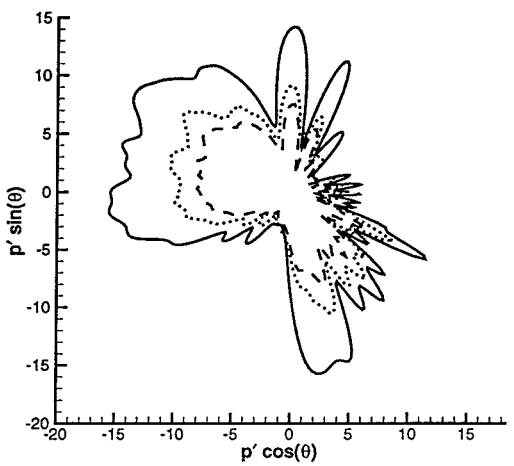

Fig. 14 Directivity of acoustic signals for $h/C \approx 0.0009$: - - -, $L_z/C = 0.25$; · · · ·, $L_z/C = 2.0$; and ——, two-dimensional calculation.

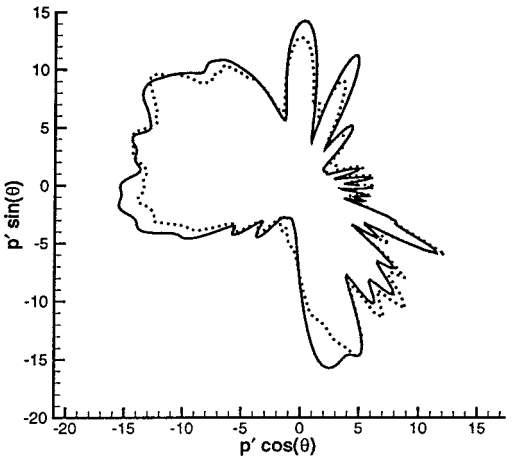

Fig. 15 Directivity of acoustic signals for $h/C \approx 0.0009$: · · · ·, L_z/C = 2.0 scaled by a factor of 1.4, and ——, two-dimensional calculation.

Although uniform scaling of the small-to-moderate L_z results does not exactly replicate the two-dimensional directivity pattern, such a simple scaling is a reasonable estimate. A comparison of the two-dimensional results and the $L_z/C = 2.0$ results scaled by a factor of 1.4 is shown in Fig. 15. The agreement between the two is surprisingly good. However, the scaling factor was determined empirically. Efforts to derive the scaling factor have been unsuccessful thus far. For instance, the ratio obtained by dividing the amplitude of the integration of Eq. (4) from $z = -\infty$ to ∞ by the amplitude of the the integration from $z = -L_z$ to L_z might be expected to approximate the scaling factor. However, this ratio is approximately 1.03, rather than the empirically determined value of 1.4. Variations on this theme, such as taking ratios of only the real or imaginary parts, produced similarly disappointing results. Additional work still needs to be done to take full advantage of the two-dimensional acoustic solution in this type of quasi-two-dimensional flow.

Conclusions

Data from highly resolved, unsteady, two-dimensional RANS calculations of a high-lift configuration with a blunted slat trailing edge were used to perform acoustic analyses with the permeable-surface FW–H equation. The results lend support to the hypothesis proposed by Khorrami et al.[15] that vortex shedding from the trailing edge of the slat is responsible for a loud, high-frequency noise observed in a corresponding set of experiments. In addition, the frequency of the high-frequency tone scales approximately with the sum of the slat trailing-edge thickness and the displacement thicknesses of the upper and lower boundary layers. A two-dimensional FW–H solver[21] was used to evaluate the noise computed from a variety of different integration surfaces. The use of an on-body integration surface produced large directivity lobes directly upstream and toward the microphone array. The use of an off-body integration surface that did not include the slat cove region produced a similar directivity pattern. However, off-body integration surfaces that did include the slat cove region produced a considerably modified directivity pattern. Further research with more controlled sources should be performed to help determine more specific guidelines for the placement of the integration surfaces. Comparison of mean-square pressure results with data from individual microphones in the acoustic array showed qualitatively similar trends.

A number of three-dimensional acoustic calculations were performed by replicating the two-dimensional RANS data in the spanwise direction for varying spanwise extents. As expected, the noise generally increased with increasing spanwise extent. All of the important directivity lobes observed in the two-dimensional acoustic results were observed at the smallest spanwise extent tested. A simple scaling of the three-dimensional directivity pattern compared favorably with the two-dimensional directivity pattern. Unfortunately, to date, the scaling factor can only be obtained empirically, after both the two-dimensional and three-dimensional cases have been computed. A method for modeling the scaling factor would greatly enhance the predictive usefulness of the two-dimensional solution. However, continued improvements in computer hardware and CFD codes hint at the possibility that well-resolved, time-dependent three-dimensional RANS calculations will become sufficiently affordable in the future so as to obviate the need for such modeling.

Acknowledgments

The authors thank Craig Streett, Robert Stoker, James Underbrink, and Guy Neubert for the use and analysis of the experimental data.

References

[1]Davy, R., and Remy, H., "Airframe Noise Characteristics on a 1/11 Scale Airbus Model," AIAA Paper 98-2335, June 1998.

[2]Hayes, J. A., Horne, W. C., Soderman, P. T., and Bent, P. H., "Airframe Noise Characteristics of a 4.7% Scale DC-10 Model," AIAA Paper 97-1594, May 1997.

[3]Dobrzynski, W., Nagakura, K., Gehlhar, B., and Buschbaum, A., "Airframe Noise Studies on Wings with Deployed High-Lift Devices," AIAA Paper 98-2337, June 1998.

[4]Macaraeg, M. G., "Fundamental Investigations of Airframe Noise," AIAA Paper 98-2224, June 1998.

[5]Meadows, K. R., Brooks, T. F., Humphreys, W. M., Hunter, W. H., and Gerhold, C. H., "Aeroacoustic Measurements of a Wing-Flap Configuration," AIAA Paper 97-1595, May 1997.

[6]Khorrami, M. R., Singer, B. A., and Takallu, M. A., "Analysis of Flap Side-Edge Flow Field for Identification and Modeling of Possible Noise Sources," Society of Automotive Engineers, Paper 971917, May 1997.

[7]Takallu, M. A., and Laflin, K. R, "Reynolds-Averaged Navier–Stokes Simulations of Two Partial-Span Flap Wing Experiments," AIAA Paper 98-0701, Jan. 1998.

[8]Streett, C. L., "Numerical Simulation of Fluctuations Leading to Noise in a Flap-Edge Flowfield," AIAA Paper 98-0628, Jan. 1998.

[9]Streett, C. L., "Numerical Simulations of a Flap-Edge Flowfield," AIAA Paper 98-2226, June 1998.

[10]Khorrami, M. R., Singer, B. A., and Radeztsky, R. H. J., "Reynolds-Averaged Navier–Stokes Computations of Flap-Side-Edge Flowfield," *AIAA Journal*, Vol. 37, No. 1, 1999, pp. 14–22.

[11]Khorrami, M. R., and Singer, B. A., "Stability Analysis for Noise-Source Modeling of a Part-Span Flap," *AIAA Journal*, Vol. 37, No. 10, 1999, pp. 1206–1212.

[12]Morgan, H. L., "Model Geometry Description and Pressure Distribution Data From Tests of EET High-Lift Research Model Equippped with Full-Span Slat and Part-Span Flaps," NASA TM-80048, 1979.

[13]Underbrink, J. R., and Dougherty, R. P., "Array Design for Non-Intrusive Measurments of Noise Sources," *Proceedings of NOISE-CON 96*, edited by J. D. Chalupnik, S. E. Marshall, and R. C. Klein, Inst. of Noise Control Engineering, Noise Control Foundation, Poughkeepsie, NY, 1996.

[14]Storms, B. L., Hayes, J. A., Moriarty, P. J., and Ross, J. C., "Aeroacoustic Measurements of Slat Noise on a Three-Dimensional High-Lift System," AIAA Paper 99-1957, May 1999.

[15]Khorrami, M. R., Berkman, M. E., Choudhari, M., Singer, B. A., Lockard, D. L., and Brentner, K. S., "Unsteady Flow Computations of a Slat with a Blunt Trailing Edge," AIAA Paper 99-1805, May 1999.

[16]Singer, B. A., Brentner, K. S., Lockard, D. P., and Lilley, G. M., "Simulation of Acoustic Scattering from a Trailing Edge," *Journal of Sound and Vibration*, Vol. 230, No. 3, 2000, pp. 541–560.

[17]Ffowcs Williams, J. E., and Hawkings, D. L., "Sound Generated by Turbulence and Surfaces in Arbitrary Motion," *Philosophical Transactions of the Royal Society of London*, Vol. A264, No. 1151, 1969, pp. 321–342.

[18]Brentner, K. S., and Farassat, F., "An Analytical Comparison of the Acoustic Analogy and Kirchhoff Formulation for Moving Surfaces," *AIAA Journal*, Vol. 36, No. 8, 1998, pp. 1379–1386.

[19]Cox, J. S., Brentner, K. S., and Rumsey, C. L., "Computation of Vortex Shedding and Radiated Sound for a Circular Cylinder: Subcritical to Transcritical Reynolds Numbers," *Theoretical and Computational Fluid Dynamics*, Vol. 12, No. 4, 1998, pp. 233–253.

[20]Rumsey, C. L., Biedron, R., Farassat, F., and Spence, P. L., "Ducted-Fan Engine Acoustic Predictions Using a Navier–Stokes Code," *Journal of Sound and Vibration*, Vol. 213, No. 4, 1998, pp. 643–664.

[21]Lockard, D. P., "An Efficient, Two-Dimensional Implementation of the Ffowcs Williams and Hawkings Equation," *Journal of Sound and Vibration*, Vol. 229, No. 4, 2000, p. 897.

[22]Hammond, D. A., and Redekopp, L. G., "Global Dynamics of Symmetric and Asymmetric Wakes," *Journal of Fluid Mechanics*, Vol. 331, 1997, pp. 231–260.

M. Samimy
Associate Editor